Applied Physics Letters

Experimental demonstration of deeply subwavelength dielectric sensing with epsilon-near-zero (ENZ) waveguides EP

Cite as: Appl. Phys. Lett. **120**, 081106 (2022); https://doi.org/10.1063/5.0079665
Submitted: 23 November 2021 • Accepted: 07 February 2022 • Published Online: 23 February 2022

Published open access through an agreement withPublished open access through an agreement with JISC Collections

Miguel Beruete, Nader Engheta and Victor Pacheco-Peña

COLLECTIONS

Note: This paper is part of the APL Special Collection on Zero-index Metamaterials for Classical and Quantum Light.

EP This paper was selected as an Editor's Pick

Applied Physics Letters ARTICLE scitation.org/journal/apl

Experimental demonstration of deeply subwavelength dielectric sensing with epsilon-near-zero (ENZ) waveguides

Cite as: Appl. Phys. Lett. **120**, 081106 (2022); doi: 10.1063/5.0079665
Submitted: 23 November 2021 · Accepted: 7 February 2022 ·
Published Online: 23 February 2022

View Online Export Citation CrossMark

Miguel Beruete,[1,2,a)] Nader Engheta,[3,a)] and Victor Pacheco-Peña[4,a)]

AFFILIATIONS

[1]Department of Electrical, Electronic and Communication Engineering, Universidad Pública de Navarra, 31006 Pamplona, Navarra, Spain
[2]Institute of Smart Cities (ISC), Public University of Navarre, Campus de Arrosadia, 31006 Pamplona, Navarra, Spain
[3]Department of Electrical and Systems Engineering, University of Pennsylvania, Philadelphia, Pennsylvania 19104, USA
[4]School of Mathematics, Statistics and Physics, Newcastle University, Newcastle Upon Tyne NE1 7RU, United Kingdom

Note: This paper is part of the APL Special Collection on Zero-index Metamaterials for Classical and Quantum Light.
[a)]**Authors to whom correspondence should be addressed:** miguel.beruete@unavarra.es; engheta@ee.upenn.edu; and victor.pacheco-pena@newcastle.ac.uk

ABSTRACT

In this Letter, an all metallic sensor based on ε-near-zero (ENZ) metamaterials is studied both numerically and experimentally when working at microwave frequencies. To emulate an ENZ medium, a sensor is made by using a narrow hollow rectangular waveguide, working near the cutoff frequency of its fundamental TE_{10} mode. The performance of the sensor is systematically evaluated by placing subwavelength dielectric analytes (with different sizes and relative permittivities) within the ENZ waveguide and moving them along the propagation and transversal axes. It is experimentally demonstrated how this ENZ sensor is able to detect deeply subwavelength dielectric bodies of sizes up to 0.04λ and height $5 \times 10^{-3}\ \lambda$ with high sensitivities (and the figure of merit) up to 0.05 1/RIU ($\sim$0.6 GHz^{-1}) and 0.6 1/RIU when considering the sensor working as a frequency- or amplitude-shift-based device, respectively.

The fields of metamaterials and metasurfaces (as their 2D version) have enabled new wave–matter interaction paradigms for arbitrary manipulation of fields and waves.[1] They have been applied in multiple applications ranging from computing,[2,3] lenses,[4,5] antennas[6,7] to invisibility cloaking[8,9] and even in applications where electromagnetic properties of media can be changed both in space and time.[10–15] In this realm, metamaterials exhibiting effective ε-near-zero (ENZ) responses have opened new opportunities for manipulation of light–matter interactions given their exotic features of near-zero propagation constant and almost infinite effective wavelength of the wave traveling through them.[16,17]

Interestingly, it was demonstrated that such artificial media can be easily emulated by exploiting the intrinsic structural dispersion of rectangular waveguides working near the cutoff frequency of their fundamental mode TE_{10}.[18] ENZ metamaterials have rapidly evolved in the recent years demonstrating their applicability in diverse scenarios such as in power splitters,[19] antennas and lenses,[7,20,21] and dielectric sensors,[22,23] among others. There are even ENZ sensors operating at visible wavelengths based on nonperiodic sodium tungsten bronze metamaterials.[24] In our previous work, we demonstrated both theoretically and numerically how narrow hollow rectangular waveguides emulating ENZ metamaterials can be used as sensors for small dielectric particles with subwavelength sizes,[25] complementing previous sensor designs[26,27] based on cutoff waveguides that did not consider ENZ operation. Inspired by the interesting features of ENZ-based sensors, in this paper, we perform the experimental and accompanying numerical demonstration of an ENZ waveguide sensor using a narrow waveguide operating near cutoff in a similar configuration as in our theoretical proposal.[25] As discussed below, this geometry has excellent sensing performance even when deeply subwavelength dielectric objects are inserted inside the channel.

The structure under test is depicted schematically in Fig. 1(a). The central element is the sensing region that consists of a narrow waveguide channel, which, according to the theory developed in Ref. 22, emulates an ENZ medium. Henceforth, this element will be referred to as the ENZ channel. The analytes (i.e., the bodies to be sensed) are small dielectric cuboids of dimensions $L_x \times L_y \times L_z$, with the L_y dimension (height) much smaller than the others, as represented in Fig. 1(b), and are inserted inside the ENZ channel at different positions to evaluate the sensing performance. The signal is injected through a standard metallic rectangular waveguide coupled to the ENZ channel, and another identical waveguide is connected at the output to guide the signal to the detector. These input and output waveguides have dimensions such that their cutoff frequency is below that of the ENZ channel, and hence, they can excite properly the ENZ-like regime inside the channel. This is visualized in the simulation results of Fig. 1(c), which are obtained with the numerical electromagnetic simulator COMSOL Multiphysics® using the frequency domain solver. The electric field (E_y) on the xz plane is obviously uniform along the z direction inside the ENZ channel, whereas it has spatial variations inside the input and output waveguides. This is a clear indication that the ENZ channel is working very near cutoff, and hence, there is practically no phase advance inside it, whereas the input and output waveguides are operating well above cutoff.

The experimental test of this structure was performed using the setup shown in the photographs of Fig. 2. It consists of two WR430 coaxial to waveguide transitions attached to rectangular waveguides of length equal to 165 mm, specifically manufactured by the CNC milling machine in a single piece to avoid power leakage. Nominally, the waveguides should have transverse dimensions of $109.22 \times 54.61\ \text{mm}^2$ according to the WR430 standard. However, due to fabrication imperfections, the final dimensions were $109.15 \times 54.55\ \text{mm}^2$, resulting in a maximum yet small error of 0.11%. Between both waveguides was attached the ENZ channel, which is another waveguide designed with transversal dimensions of $62.81 \times 0.98\ \text{mm}^2$ and length 20 mm with

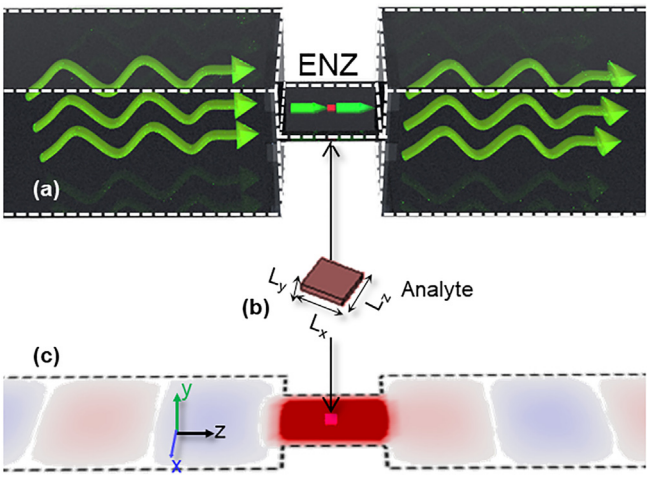

FIG. 1. Schematic representation of the ENZ sensor. (a) Narrow hollow rectangular waveguide emulating an ENZ medium connected in between two rectangular waveguides. (b) Electric field distribution on the xz plane. The red square is the dielectric analyte to be sensed.

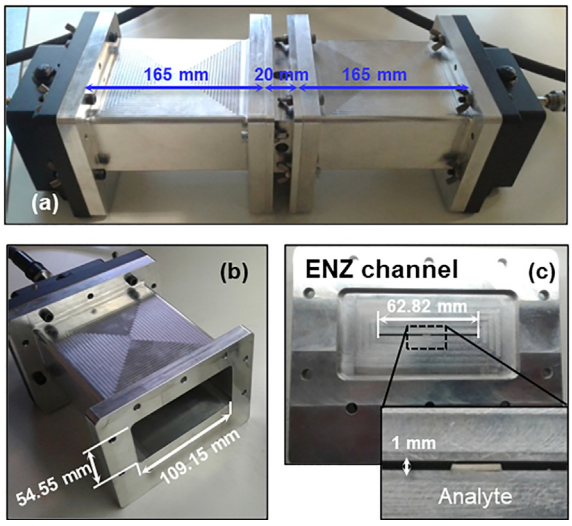

FIG. 2. Constructed ENZ sensor. (a) Photograph of the complete structure with all pieces attached. (b) Photograph of the lateral input and output waveguides. (c) Front view of the ENZ channel. (Inset) Photograph showing the analyte inside of the ENZ channel.

final dimensions of $62.82 \times 1\ \text{mm}^2$ due to fabrication imperfections. As it will be shown below, the sensor was evaluated by moving small dielectric analytes inside the ENZ channel. To do this, small holes of diameter 0.95 mm were drilled at the center of the ENZ channel: one on the top, left, and right-hand sides. These holes where used to move the analyte within the ENZ channel without perturbing the field distribution inside the sensor. Finally, the cutoff frequency obtained from the manufactured dimensions is ~1.37 GHz for the input and output waveguides and ~2.39 GHz for the ENZ channel. Nevertheless, according to the WR430 standard, the recommended band starts at 1.7 GHz, which is still below the cutoff frequency of the ENZ channel, as required to excite properly the ENZ regime inside it.

The experimental characterization was done by connecting the coaxial-to-waveguide transitions to an Agilent 8722ES vector network analyzer. Measurements were taken from 1.5 to 3.5 GHz (although in the plots we only show the band from 2 to 2.6 GHz for clarity and also for the fact that this band includes the 2.39 GHz ENZ frequency as the cutoff of the ENZ channel) with a frequency step of 1.25 MHz. To get an accurate response, waveguide TRL calibration was applied using a waveguide short and two offsets of length 1/4 and 1/8 of the free-space wavelength at the center frequency of the S-band (2.5 GHz). With this method, the whole setup is calibrated up to the aperture of the metallic waveguides, and therefore, the S-parameters of the ENZ channel can be measured with reduced (almost negligible) errors. The sensing performance was analyzed by inserting dielectric cuboids inside the ENZ channel. These analytes were obtained by trimming small pieces from commercial substrates[28] with permittivity and height as shown in Table I, $L_z = 5$ mm, and three different widths, namely, $L_x = 5$, $L_x = 20$, and $L_x = 60$ mm.

In Figs. 3(a)–3(c), the experimental results (solid lines) compared with the numerical simulations (markers) obtained using the frequency domain solver of CST Studio Suite® are represented, showing excellent agreement, except for a slight discrepancy in the maximum

TABLE I. Characteristics of the analytes (consisting of commercial substrate materials) used for the experimental characterization.

Reference	ε_d	$\tan\delta$	L_y (mm)
RO5880	2.2	0.0009	0.787
RO3006	6.15	0.002	0.635
RO3010	10.2	0.0022	0.635

peak amplitude, which is smaller in the experiment, probably due to an underestimation of the loss tangent in simulations. When the ENZ channel is empty, a resonant peak near the theoretical resonance frequency $f_{ENZ,0} = 2.37$ GHz (with both simulation and experimental values of $f_{ENZ,0} = 2.386$ GHz) is noticed in the spectrum, see the black curve in Figs. 3(a)–3(c). This peak corresponds to the ENZ regime inside the channel.[25,29] When an analyte is inserted, the peak undergoes a clear redshift. It is noteworthy that the ENZ sensor is able to detect a deep-subwavelength dielectric body with transverse dimensions of just 0.04λ and height $5 \times 10^{-3}\ \lambda$ (where $\lambda = 125.7$ mm is the free-space wavelength at the ENZ resonance) with a relatively small permittivity of 2.2, see the red curve of panel (a). The peak shift is larger as the width of the analyte is increased. In addition, comparing the peak positions in Figs. 3(a)–3(c), it is clear that larger permittivity leads to a larger shift. Both results are in good agreement with the analytical results presented in our previous work, where an analyte covering the whole y dimension within the ENZ channel was studied.[25] A detailed evolution of the peak shift is presented as red curves in Figs. 3(d)–3(f) for both simulation (dashed lines with markers) and experimental (solid lines) results with excellent agreement. The most abrupt frequency shift happens between 5 and 20 mm widths with a gentler slope between 20 and 60 mm in all cases. As expected, the largest frequency shift occurs for the analyte with highest permittivity [Fig. 3(f)], reaching a minimum frequency of ~2.05 GHz (which is a fractional shift of ~13.8%). In the same panels [Figs. 3(d)–3(f)], the value of the transmission coefficient at 2.386 GHz (the ENZ peak frequency of the empty waveguide) is represented in blue. Obviously, the magnitude decreases as the peak shifts with the most abrupt change for small widths. This fact can be used to perform sensing based on the amplitude at a fixed frequency, instead of detecting a frequency shift, as proposed in Ref. 30.

To evaluate numerically the performance of the ENZ sensor, we use the sensitivity and figure of merit (FOM). Here, we will analyze both the frequency shift and the amplitude shift, so we need to define two different sensitivities. We define the frequency sensitivity (FS) as

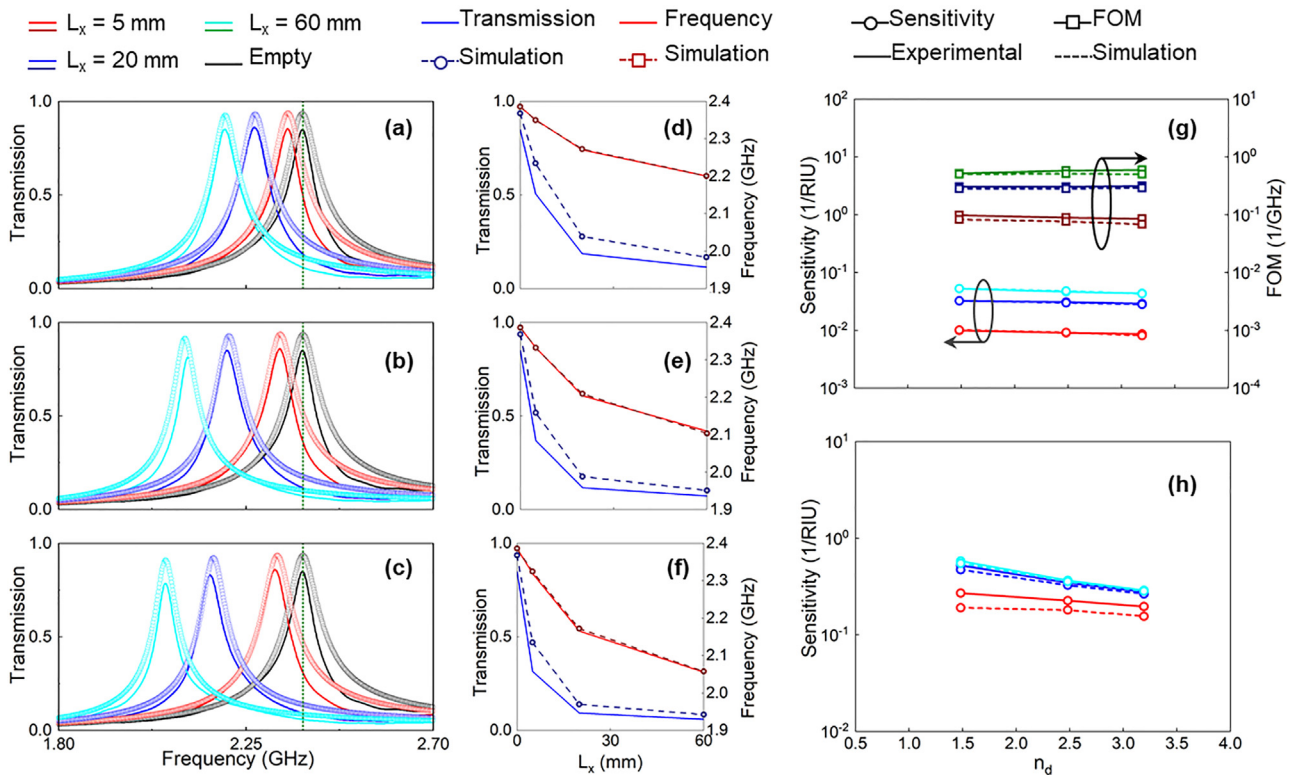

FIG. 3. Experimental (solid) and numerical (symbols) results of the transmission coefficient when the width of the analyte is: $L_x = 5$ mm (red), $L_x = 20$ mm (blue), $L_x = 60$ mm (cyan) along with the results of the empty channel (black) when the relative permittivity of the analyte is: (a) $\varepsilon_d = 2.2$, (b) $\varepsilon_d = 6.15$, and (c) $\varepsilon_d = 10.2$. (d)–(f) Frequency of each ENZ peak (red) extracted from panels (a)–(c) and the amplitude at the ENZ peak of the empty channel (blue). The experimental and numerical values are plotted as solid and dashed lines, respectively. (g) and (h) Sensitivity (bottom lines) and FOM (top lines) calculated in terms of the shift of the wavelength and refractive index (g) of the analyte along with the results using the shift of amplitude at the ENZ frequency of the empty channel (h). The experimental and numerical results are plotted as solid and dashed lines, respectively.

the fractional frequency shift of the ENZ resonance divided by the analyte refractive index: $FS = \Delta f/(f_{ENZ,0} \cdot n_d)$ [1/RIU], where $\Delta f = |f_{ENZ} - f_{ENZ,0}|$, with f_{ENZ} being the ENZ peak resonance frequency when the analyte is inserted within the sensing region, $n_d = \sqrt{\varepsilon_d}$ is the analyte refractive index, and RIU stands for refractive index unit. Similarly, the amplitude sensitivity (AS) is defined as the fractional variation of the amplitude at $f_{ENZ,0}$ divided by the analyte refractive index being: $AS = \Delta A/(A_{ENZ,0} \cdot n_d)$ [1/RIU], where $\Delta A = |A_{ENZ} - A_{ENZ,0}|$ and $A_{ENZ,0}$ and A_{ENZ} are the transmission amplitudes evaluated at $f_{ENZ,0}$ for the empty waveguide and analyte inserted, respectively. As shown in Fig. 3(g), the maximum value of FS in all the considered cases corresponds to $L_x = 60$ mm (cyan curve) as expected, as it leads to the maximum frequency shift, and decreases for smaller widths. In addition, the FS is slightly larger for small values of n_d, indicating that the change is more abrupt for small permittivity and tends to saturate for larger values. It is noteworthy that AS is larger than the FS values. The largest AS is also obtained for $L_x = 60$ mm and $n_d = 1.5$ (cyan curve) although it practically coincides with the value of $L_x = 20$ mm and $n_d = 1.5$ (blue curve). The FOM is a more accurate parameter to evaluate the sensing performance based on the frequency shift. The FOM takes into account the spectral selectivity of the resonance so that clear detection thresholds can be defined. Therefore, high quality factor resonances with narrow full-width at half-maximum (FWHM) values are obviously preferable. The FOM is defined as $FOM = FS/FWHM$ [1/GHz]. As depicted in Fig. 3(g), the FOM follows a similar trend as the sensitivity with larger values with increasing L_x.

In the next study, we evaluated the robustness of the ENZ sensor with respect to different positions of the analyte along the propagation axis (z axis). Analytes of different widths were considered ($L_x = 5$, 10, 20, 40, and 60 mm) with $L_z = 5$ mm, and the permittivities and heights are shown in Table I. As in Ref. 25, they were shifted from the central position ($z = 0$) to a position $z = \Delta_z(L/2 - L_z/2)$, where $L = 20$ mm is the length of the ENZ channel and $|\Delta_z| = 0$; 1 means that the analyte is at its center ($z = 0$ mm) or at the extremes [see the schematic representation in Fig. 4(m) to guide the eye]. Here, the analyte was shifted from $\Delta_z = \pm 1$ with a step of $\Delta_z = 0.33$. The results are shown as contour plots in Fig. 4 as a function of frequency and shift Δ_z, showing how all the analytes are detected by the sensor, and the peak of transmission remains at the same frequency for all the considered analyte shifts along the z axis. This demonstrates that the ENZ sensor has a robust response, largely insensitive to the position of the analyte along the propagation axis. This is in agreement with the analytical and numerical results described in Refs. 22, 25, and 31 and demonstrates experimentally that the field distribution along the guide axis ($x = 0$) at the ENZ resonance is practically uniform.[32,33]

The ENZ sensor is strongly sensitive to a shift of the analyte along the transverse x axis, as demonstrated in Fig. 5. The response was evaluated for analytes of width $L_x = 5$ mm with two different lengths ($L_z = 5$ and 20 mm) and the permittivities and heights shown in Table I. Similar to Fig. 4, the analytes were moved along the x axis (at $z = 0$) to a position $x = \Delta_x(b/2 - L_x/2)$ where $b = 62.82$ mm is the width of the ENZ channel and $\Delta_x = 0$; -1 means that the analyte is at its center ($x = 0$ mm) or at the lateral extreme, see the schematic representations as insets in Fig. 5. All the analytes can be detected when they are placed at the center of the sensor $\Delta_x = 0$, but as they are shifted toward the edge, the ENZ peak approaches gradually to the case of an empty channel. The extreme case occurs when $\Delta_x = -1$ for which the

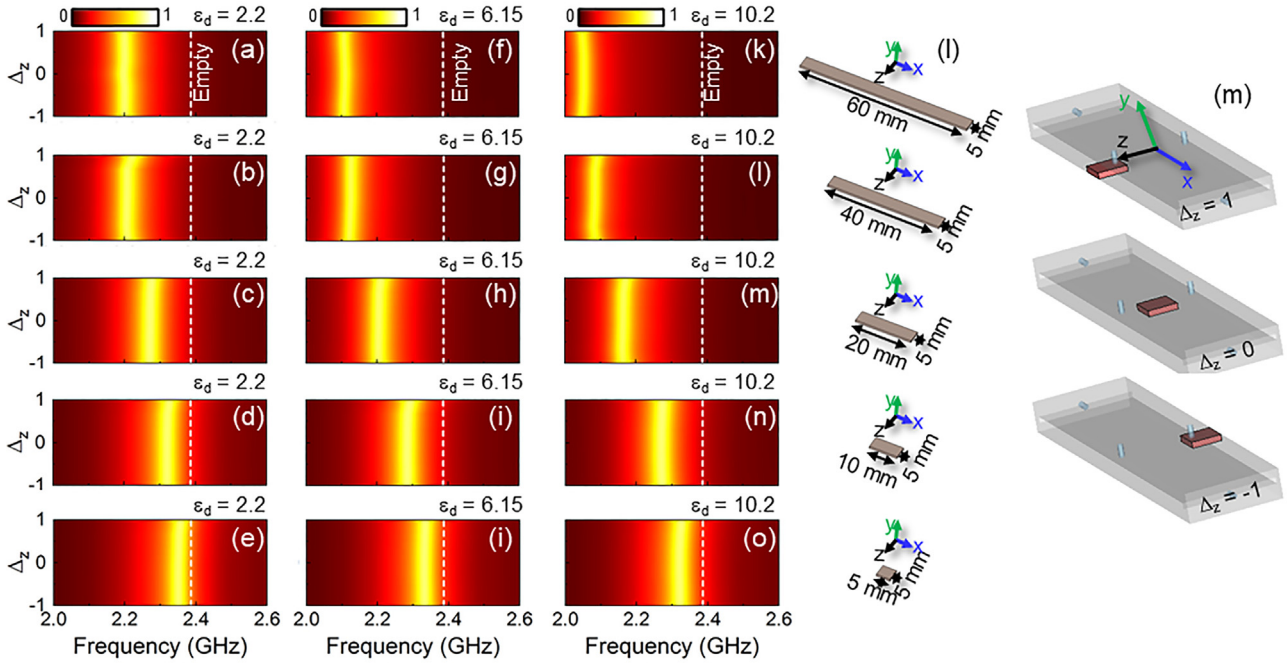

FIG. 4. Experimental results of the transmission coefficient spectra when the analyte is moved along the z axis using the three different dielectric analytes with different values of L_x (the schematic representation of each width and schematic of how the position is changed are shown in the fourth and last columns, respectively. (a)–(e) $\varepsilon_d = 2.2$. (f)–(j) $\varepsilon_d = 6.15$. (k)–(o) $\varepsilon_d = 10.2$.

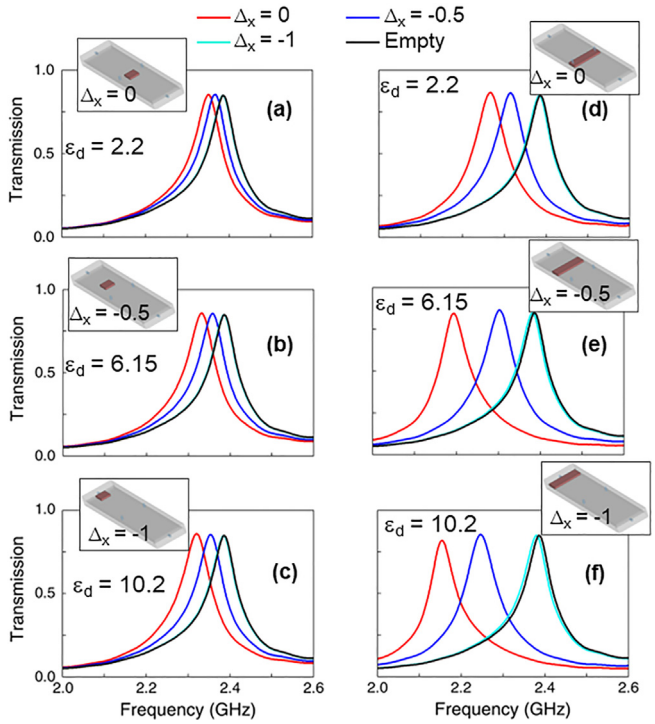

FIG. 5. Experimental results of the transmission coefficient for the case when the analyte is moved along the *x* axis. The three analytes are evaluated with $\varepsilon_d = 2.2$ (a) and (d), $\varepsilon_d = 6.15$ (b) and (e), and $\varepsilon_d = 10.2$ (c) and (f) with transverse dimensions $L_x = 5$ mm and $L_z = 5$ mm (a)–(c) along with the case of $L_x = 5$ mm and $L_z = 20$ mm (d)–(f). The positions of the analyte along the *x* axis are shown as insets to guide the eye.

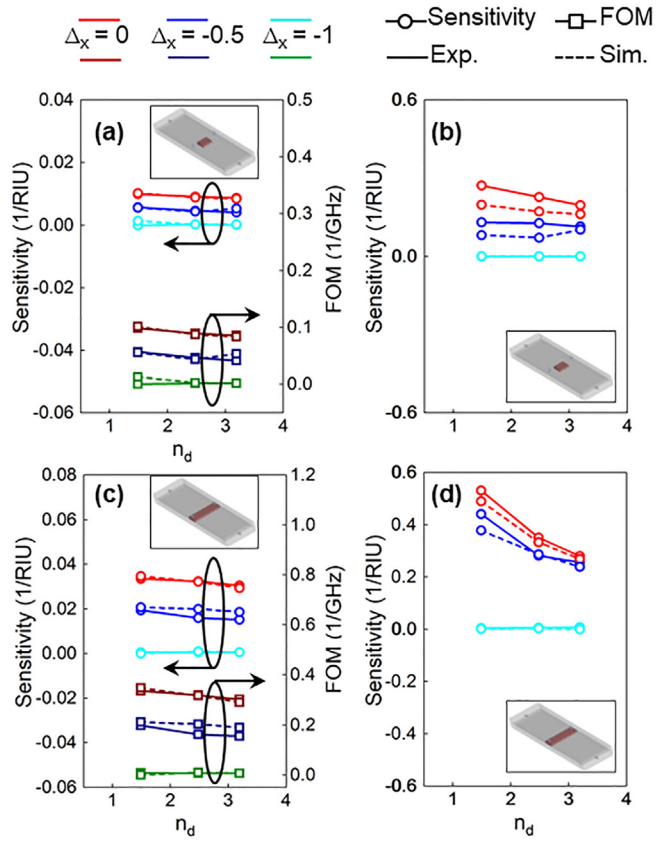

FIG. 6. Sensitivity (top lines) and FOM (bottom lines) in terms of the shift of the ENZ peak frequency (a) and (c) and the sensitivity in terms of the amplitude at f_{ENZ} (b) and (d) calculated from Fig. 5 for the case of the small analyte with $L_x = 5$ mm, $L_z = 5$ mm (a) and (b) and the analyte completely filling the z axis with $L_x = 5$ mm, $L_z = 20$ mm (c) and (d). The experimental and numerical values are shown as solid and dashed lines, respectively. The schematic representation of the analyte is shown as an inset to guide the eye.

measured transmission coefficient almost overlaps with the case of the empty channel, regardless the length of the analyte. It is also observed that the frequency shift is much more pronounced for the case $L_z = 20$ mm, in which the analyte fills completely the length of the ENZ channel, as expected. These results are in excellent agreement with the results shown in Ref. 25 and can be explained by noting that the electric field vanishes near the lateral metallic walls of the ENZ channel, and therefore, there is no interaction with the analyte at these positions. For the sake of compleneteness, from these results, we can obtain both the *FS* and *AS* as well as the *FOM* and compare the values with the simulation results, see Fig. 6. Excellent agreement between the experimental and numerical values is evident. For the case of the small analyte with $L_z = 5$ mm, Fig. 6(a), the *FS* is very small, since the peak is hardly shifted from the empty position. Both the *FS* and *FOM* increase when the analyte fills completely the z axis, Fig. 6(c), as expected, as in this case the peak shift is much larger. Again, we note that the *AS* is, in general, larger, see Figs. 6(b) and 6(d).

Regarding the specificity of the proposed sensor and the question of how to best extract the size (say volume) and refractive index of the analytes, it is worth recalling that, as discussed in our previous paper,[25] the response of a finite size analyte can be approximated with good accuracy by a slab filling completely the ENZ channel with homogenized permittivity. Therefore, in principle, there are many combinations of size and permittivity that would give similar response. Hence, one has to know in advance either the size or the permittivity of the analyte to determine the other parameter. Once this condition is fulfilled, the sensor response is largely specific provided the positioning along the x axis is known with good precision, as demonstrated by the analytical results of the previous paper and the experimental results of this paper.

To sum up, we have experimentally demonstrated a waveguide ENZ sensor able to detect deep subwavelength dielectric bodies of sizes as small as 0.04λ and height $5 \times 10^{-3}\ \lambda$. Two different detection schemes have been demonstrated: one based on the frequency shift of the ENZ resonance peak and another based on the amplitude variation at the ENZ resonance frequency of the empty waveguide. Both strategies are effective for sensing purposes and achieve high sensitivities (and the figure of merit) up to 0.05 1/RIU ($\sim$0.6 GHz^{-1}) and 0.6 1/RIU, respectively. Further studies have demonstrated the insensitivity of the ENZ sensor to different analyte positions along the ENZ channel axis, accounting for a nearly uniform electric field in this direction. Conversely, a strong variation of the response is noticed when the analyte is shifted along the transverse direction, explained by

the electric field variation in this direction due to the boundary conditions imposed by the metallic waveguide walls. All the experimental measurements are in excellent agreement with both numerical simulations and theoretical calculations obtained previously. These results could open alternative ways to develop high sensitivity sensors operating at microwaves based on metallic waveguides.

This work was supported by MCIN/AEI/10.13039/501100011033/FEDER "Una manera de hacer Europa" via Project No. RTI2018-094475-B-I00. V.P.-P. acknowledges the support from Newcastle University (Newcastle University Research Fellowship).

AUTHOR DECLARATIONS

Conflict of Interest

N.E. is a strategic scientific advisor/consultant to Meta Materials, Inc. The authors declare no conflict of interest.

DATA AVAILABILITY

The data that support the findings of this study are available from the corresponding authors upon reasonable request.

REFERENCES

[1]N. Engheta and R. W. Ziolkowski, *Metamaterials: Physics and Engineering Explorations* (John Wiley & Sons, 2006).
[2]F. Zangeneh-Nejad, D. L. Sounas, A. Alù, and R. Fleury, Nat. Rev. Mater. **6**, 207 (2021).
[3]N. Mohammadi Estakhri, B. Edwards, and N. Engheta, Science **363**, 1333 (2019).
[4]S. Legaria, J. Teniente, S. Kuznetsov, V. Pacheco-Peña, and M. Beruete, Adv. Photonics Res. **2**, 2000165 (2021).
[5]K. C. Chen, J. W. Yang, Y.-C. Yang, C. F. Khin, and M. N. M. Kehn, Opt. Express **25**, 27405 (2017).
[6]E. Lier, D. H. Werner, C. P. Scarborough, Q. Wu, and J. A. Bossard, Nat. Mater. **10**, 216 (2011).
[7]J. C. Soric, N. Engheta, S. MacI, and A. Alu, IEEE Trans. Antennas Propag. **61**, 33 (2013).
[8]D. Shin, Y. Urzhumov, Y. Jung, G. Kang, S. Baek, M. Choi, H. Park, K. Kim, and D. R. Smith, Nat. Commun. **3**, 1213 (2012).
[9]B. Orazbayev, N. Mohammadi Estakhri, M. Beruete, and A. Alù, Phys. Rev. B **91**, 195444 (2015).
[10]V. Pacheco-Peña and N. Engheta, Light Sci. Appl. **9**, 129 (2020).
[11]H. Li, H. Moussa, D. Sounas, and A. Alù, Phys. Rev. Appl. **14**, 031002 (2020).
[12]V. Pacheco-Peña and N. Engheta, Optica **7**, 323 (2020).
[13]P. A. Huidobro, E. Galiffi, S. Guenneau, R. V. Craster, and J. B. Pendry, Proc. Natl. Acad. Sci. **116**, 24943 (2019).
[14]V. Pacheco-Peña and N. Engheta, Nanophotonics **9**, 379 (2020).
[15]D. Ramaccia, A. Alù, A. Toscano, and F. Bilotti, Appl. Phys. Lett. **118**, 101901 (2021).
[16]M. G. Silveirinha and N. Engheta, Phys. Rev. B **76**, 245109 (2007).
[17]I. Liberal and N. Engheta, Nat. Photonics **11**, 149 (2017).
[18]A. Alù, M. G. Silveirinha, and N. Engheta, Phys. Rev. E **78**, 016604 (2008).
[19]V. Pacheco-Peña, V. Torres, M. Beruete, M. Navarro-Cía, and N. Engheta, J. Opt. (United Kingdom) **16**, 094009 (2014).
[20]C. Della Giovampaola and N. Engheta, Nat. Mater. **13**, 1115 (2014).
[21]V. Torres, V. Pacheco-Peña, P. Rodríguez-Ulibarri, M. Navarro-Cía, M. Beruete, M. Sorolla, and N. Engheta, Opt. Express **21**, 9156 (2013).
[22]A. Alù and N. Engheta, Phys. Rev. B **78**, 045102 (2008).
[23]A. K. Jha and M. J. Akhtar, IEEE Trans. Microwave Theory Tech. **63**, 2418 (2015).
[24]Z. Fusco, M. Taheri, R. Bo, T. Tran-Phu, H. Chen, X. Guo, Y. Zhu, T. Tsuzuki, T. P. White, and A. Tricoli, Nano Lett. **20**, 3970 (2020).
[25]V. Pacheco-Peña, M. Beruete, P. Rodríguez-Ulibarri, and N. Engheta, New J. Phys. **21**, 043056 (2019).
[26]B. A. Galwas, J. K. Piotrowski, and J. Skulski, IEEE Trans. Instrum. Meas. **46**, 511 (1997).
[27]T. Shimizu and Y. Kobayashi, IEICE Trans. Electron. **E87–C**, 672 (2004).
[28]See https://www.rogerscorp.com/ for "Rogerscorp" (n.d.).
[29]V. Pacheco-Peña, V. Torres, B. Orazbayev, M. Navarro-cía, M. Beruete, and N. Engheta, in Optics and Photonics New, December 2015, p. 35, https://www.optica-opn.org/home/articles/volume_26/december_2015/extras/advances_in_%CE%B5-near-zero_metamaterial_devices/.
[30]I. Jáuregui-López, P. Rodríguez-Ulibarri, S. A. Kuznetsov, N. A. Nikolaev, and M. Beruete, Sensors (Basel) **18**, 3848 (2018).
[31]V. Pacheco-Peña, M. Navarro-Cía, and M. Beruete, Opt. Laser Technol. **80**, 162 (2016).
[32]B. Edwards, A. Alù, M. Young, M. Silveirinha, and N. Engheta, Phys. Rev. Lett. **100**, 033903 (2008).
[33]V. Pacheco-Peña, N. Engheta, S. Kuznetsov, A. Gentselev, and M. Beruete, Phys. Rev. Appl. **8**, 034036 (2017).